Chiral Grayscale Imaging with Plasmonic Metasurfaces of Stepped Nanoapertures

Yang Chen, Jie Gao,* and Xiaodong Yang*

Optical chiral imaging, as an important tool in chemical and biological analysis, has recently undergone a revolution with the development of chiral metamaterials and metasurfaces. However, the existing chiral imaging approaches based on metamaterials or metasurfaces can only display binary images with 1 bit pixel depth having either black or white pixels. Here, the unique chiral grayscale imaging based on plasmonic metasurfaces of stepped V-shaped nanoapertures is reported with both high circular dichroism and large polarization linearity in transmission. By interlacing two subarrays of chiral nanoaperture enantiomers into one metasurface, two specific linear polarization profiles are independently generated in transmission under different incident handedness, which can then be converted into two distinct intensity profiles for demonstrating spin-controlled grayscale images with 8 bit pixel depth. The proposed chiral grayscale imaging approach with subwavelength spatial resolution and high data density provides a versatile platform for many future applications in image encryption and decryption, dynamic display, advanced chiroptical sensing, and optical information processing.

1. Introduction

Optical imaging, as a key research area in photonic science and technology, covers a broad range from human eyes, to digital cameras, microscopes, and even to astronomical telescopes.[1] In the past decades, benefiting from the modern nanofabrication techniques, optical metamaterials and metasurfaces have been extensively utilized to fulfill the increasing requirements of miniaturization and integration for optical imaging devices.[2–9] Compared to the traditional imaging techniques, metamaterials and metasurfaces can overcome the diffraction limit and generate optical images with higher spatial resolution, and improved data density, device compactness, and image stability. Recently, chiral imaging approaches based on chiral metamaterials and metasurfaces have drawn special attention for the potential applications in chemical and biological analysis,[10–17] because the majority of biologically important chemical specials

are chiral, such as amino acids, nucleic acids, and carbohydrates.[18,19] During the image encoding process, chiral nanostructures in two enantiomeric forms are spatially arranged as image pixels, which possess different output intensities for right-handed and left-handed circularly polarized (RCP and LCP) light. Depending on the incident handedness, the pixels are locally switched on or off to display different image patterns. However, most of the existing chiral imaging approaches based on metamaterials or metasurfaces can only create binary images with 1 bit pixel depth allowing two colors of black and white, while the data density and image quality are also highly restricted.[10,12–15]

One straightforward scheme to achieve chiral grayscale imaging with higher bit pixel depths is to employ a series of chiral nanostructures with continuously modulated circular dichroism to encode the image. However, this method requires delicate adjustment for the geometric parameters of nanostructure unit cells,[20–23] which is quite challenging in both simulation and fabrication. Alternatively, the output polarization state of each nanostructure unit cell can be introduced as a new degree of freedom to control the shades of gray for generating grayscale images.[24,25] In such design, the nanostructures with linearly polarized transmission or reflection are spatially arranged with tailored orientation angles to generate a spatially variant linear polarization profile under linearly polarized incidence, and then the desired intensity profile is converted through an analyzer of linear polarizer following the Malus' law. For this approach, it remains a great challenge to design chiral nanostructures with simultaneously high circular dichroism and large output polarization linearity for achieving incident handedness-dependent grayscale images. If we use the circular Jones transmission matrix T_{circ} to characterize the transmission properties of the designed chiral nanostructure unit cell under circular polarization basis[26]

$$\begin{pmatrix} t_R \\ t_L \end{pmatrix} = T_{circ} \begin{pmatrix} i_R \\ i_L \end{pmatrix} = \begin{pmatrix} T_{RR} & T_{RL} \\ T_{LR} & T_{LL} \end{pmatrix} \begin{pmatrix} i_R \\ i_L \end{pmatrix} \qquad (1)$$

the strictly required condition is $T_{RR} = T_{LR} \gg T_{RL} = T_{LL}$ or $T_{RL} = T_{LL} \gg T_{RR} = T_{LR}$. Furthermore, 3D chiral nanostructures with arbitrary rotational angles are difficult to fabricate, while planar chiral nanostructures are not truly chiral and hence suffer from weak chiroptical responses.[27,28]

Dr. Y. Chen, Prof. J. Gao, Prof. X. Yang
Department of Mechanical and Aerospace Engineering
Missouri University of Science and Technology
Rolla, MO 65409, USA
E-mail: gaojie@mst.edu; yangxia@mst.edu

The ORCID identification number(s) for the author(s) of this article can be found under https://doi.org/10.1002/adom.201801467.

In this work, we propose plasmonic stepped V-shaped nanoapertures as a new type of chiral nanostructures with both high circular dichroism and large polarization linearity to construct metasurfaces for demonstrating chiral grayscale subwavelength imaging. Transformed from the V-shaped nanoaperture with uniform depth, the stepped V-shaped nanoaperture with arbitrary orientation angle having truly 3D chirality can be easily fabricated. Circular dichroism in transmission as high as 0.81 is experimentally achieved with the transmitted light linearly polarized along a certain direction, which is attributed to the spin-dependent mode coupling process inside the nanostructure. By interlacing two independent subarrays based on the two enantiomers of the chiral nanostructure into one metasurface, chiral grayscale subwavelength imaging is enabled to produce two distinct grayscale images with 8 bit pixel depth and subwavelength spatial resolution for different incident handedness. Mutual disturbance between the two subarrays is effectively prohibited. Furthermore, the dependence of the captured images on the output polarization as well as the operation wavelength is also discussed. Our approach promises plenty of potential applications in image

encryption and decryption,[29] dynamic display,[30] chiroptical biosensing,[31] and optical information processing.[32]

2. Results and Discussion

2.1. Design of Chiral Nanostructure Unit Cell

In order to achieve high circular dichroism and linearly polarized transmission simultaneously, plasmonic stepped V-shaped nanoapertures milled in an optically thick gold film are proposed as chiral nanostructure unit cells (**Figure 1**a). The stepped V-shaped nanoaperture is evolved from the well-known V-shaped nanoaperture with uniform depth,[3,33] which possesses mirror symmetry in both x–y and y–z planes and thus exhibits no optical chirality. By selectively truncating the right or left half of the V-shaped nanoaperture, stepped V-shaped nanoapertures lacking any mirror symmetry are constructed in Form A or Form B. Distinguished from planar chiral nanostructures, symmetry breaking is also introduced along the propagation direction to result in a truly chiral geometry. On
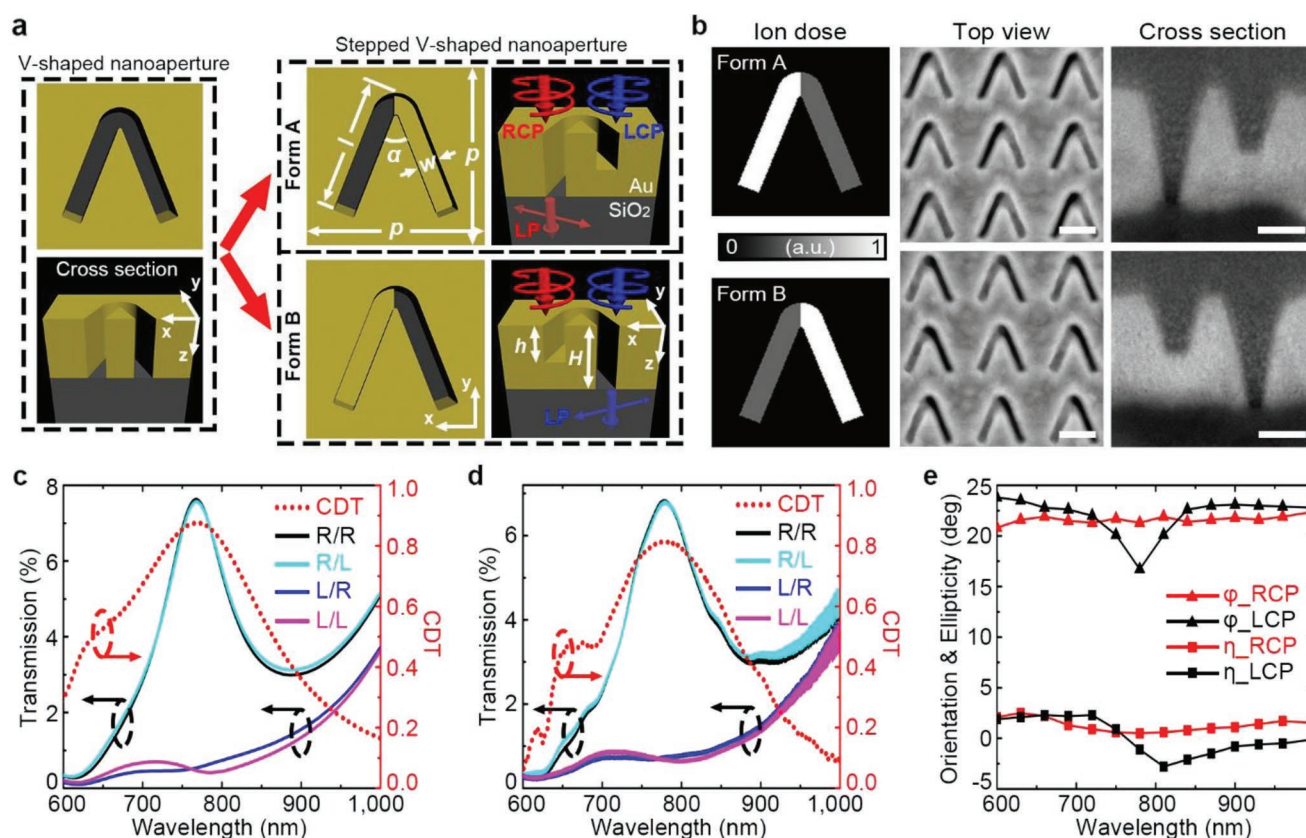

Figure 1. Design, fabrication, and optical characterization of the chiral stepped V-shaped nanoaperture. a) Illustration of the transformation process from an achiral V-shaped nanoaperture to the chiral stepped V-shaped nanoaperture in its two enantiomeric forms (Form A and Form B). Geometric parameters of the stepped V-shaped nanoapertures are optimized as: $p = 400$ nm, $l = 300$ nm, $w = 50$ nm, $\alpha = 43°$, $H = 180$ nm, and $h = 100$ nm. b) Normalized ion dose distributions and SEM images of the stepped V-shaped nanoaperture in its two forms fabricated using the grayscale focused ion beam milling method. The cross-section images are obtained with a visual angle of 42° to the surface normal. The scale bars are 200 and 50 nm from left to right. c) Simulated and d) measured transmission spectra of the stepped V-shaped nanoaperture array in Form A for different incident/transmitted handedness combinations together with the corresponding CDT spectra. R/L refers to the LCP transmission under RCP incidence and the other three components (R/R, L/R, and L/L) are defined in the same way. e) Measured orientation angle φ and ellipticity angle η of the output polarization for the stepped V-shaped nanoaperture array in Form A under RCP and LCP incidence.

the other hand, compared to conventional 3D chiral nanostructures with fabrication difficulties, the stepped V-shaped nanoapertures can be easily fabricated with arbitrary orientation angles using one-step grayscale focused ion beam milling method (Figure 1b). Different ion doses are applied at the two halves of nanoaperture to produce different milling depths. High fabrication uniformity is demonstrated in Figure 1b. It is noted that the realistic sidewalls of nanoaperture are tapered instead of vertical as expected, whose influence is discussed in Figure S2 Supporting Information.

The optical properties of the stepped V-shaped nanoapertures are investigated by full-wave electromagnetic simulations. It is seen that a pronounced transmission resonance appears at 768 nm under RCP incidence, while the transmission under LCP incidence around this wavelength is strongly prohibited for the stepped nanoaperture in Form A (Figure 1c). The corresponding circular dichroism in transmission (CDT) $= (T_R - T_L)/(T_R + T_L)$ is calculated to be 0.88, where $T_R = T_{R/R} + T_{R/L}$ and $T_L = T_{L/R} + T_{L/L}$. The measured CDT resonance of 0.81 at 780 nm matches well with the simulation (Figure 1d). Meanwhile, the RCP and LCP components among the transmitted light of RCP incidence have almost equal intensity as revealed in both simulation and experiment (Figure 1c,d). Large polarization linearity in transmission is obtained with the measured polarization ellipticity angle η below 2.5° over a broad spectrum from 600 to 1000 nm (Figure 1e). The retrieved components of circular Jones transmission matrix T_{circ} from simulation are $T_{RR} = 0.324e^{2.8i}$, $T_{RL} = 0.322e^{-1.0i}$, $T_{LR} = 0.089e^{-2.2i}$, and $T_{LL} = 0.089e^{0.53i}$, which fulfill well the aforementioned requirements for designing the chiral nanostructure unit cell. Besides, the orientation angle φ of the linearly polarized transmitted light for RCP incidence is kept around 21.5°, which is approximately orthogonal to the left half of the stepped V-shaped nanoaperture in Form A (Figure 1e).

2.2. Chiroptical Analysis

To reveal the underlying mechanism of the unique optical properties for the stepped V-shaped nanoaperture, we first consider the V-shaped groove structure (**Figure 2**a). For plane wave excitation polarized along the x-direction, a high-energy antisymmetric localized mode is excited inside the V-shaped groove structure as suggested by the reflection dip at 644 nm (Figure 2a). Correspondingly, electric dipoles induced in the two halves are out of phase with each other (Figure 2b). But for y-polarized incident wave, a low-energy symmetric mode is excited at 850 nm, where the two electric dipoles oscillate in phase to each other. When RCP or LCP wave is illuminated, the antisymmetric and symmetric modes are simultaneously excited with a relative phase delay of $\pi/2$ or $-\pi/2$, leading to constructive field interference at the left half and destructive field interference at the right half for the RCP case and vice versa for the LCP case (Figure 2b). The field interference is resonant at 768 nm where the antisymmetric and symmetric modes have the largest spectral overlap,[34] resulting in highly spin-dependent field distributions where the electric field at the left (right) half is significantly stronger than that at the right (left) half for the RCP (LCP) case (Figure 2a,b).

Next, the stepped V-shaped nanoaperture in Form A can be considered as a V-shaped groove structure at the top layer connected on the left with a rectangular aperture at the bottom layer. When circularly polarized wave is illuminated, plasmonic modes are excited inside the top-layer groove structure and then coupled to the fundamental TE_{10} mode of the bottom-layer rectangular aperture,[35] which is the only propagation mode for the rectangular aperture at the spectrum range from 600 to 1000 nm. The radiation linear polarization of the TE_{10} mode is kept normal to the rectangular aperture. Due to the circularly dichroic field distributions of the V-shaped groove structure, the TE_{10} mode excited inside the bottom-layer rectangular aperture under RCP incidence is much stronger than that under LCP incidence (Figure 2c). High circular dichroism in transmission is thus achieved. **Figure 3**d shows optical power flow distributions. It is clearly observed that the incoming RCP wave is selectively focused into the left channel and transmitted through the gold film, while the LCP wave is converged into the right channel and then reflected back by the truncated surface. In brief, the stepped V-shaped nanoaperture can be treated as a two-channel optical spin filter cascaded by a photon extractor to switch on either the left or right channel.

2.3. Metasurface Design

The metasurface for chiral grayscale subwavelength imaging is then designed with the chiral stepped V-shaped nanostructures with linearly polarized transmission. Two subarrays consisting respectively of the two enantiomers of the stepped V-shaped nanoaperture are independently designed for producing the grayscale portrait images of Einstein and Curie, which are then interlaced and merged into a single metasurface (Figure 3a). The unit cell period of each subarray p is enlarged to 566 nm, and the displacement vector during the merging process is ($p/2$, $p/2$), so that the equivalent unit cell period remains 400 nm for the merged metasurface. The distance between neighboring unit cells is large enough to avoid the influence of near-field coupling (see Figure S3, Supporting Information). The overall size of the merged metasurface is 169 μm × 169 μm. When the merged metasurface is illuminated by a RCP beam, the transmission of subarray B is almost totally suppressed, while the transmission of subarray A is allowed to generate a spatially varying linear polarization profile with uniform intensity. The local polarization direction is determined by the orientation angle of nanoaperture. Since normal image sensors like human eyes and charge-coupled devices (CCDs) are insensitive to the polarization information of light, an analyzer of linear polarizer is utilized after the metasurface to convert the linear polarization profile to the intensity profile (Figure 3b). According to the Malus' law, when a linearly polarized light is incident on an analyzer, the intensity of the transmitted light is directly proportional to the square of the cosine of angle between the transmission axis of the analyzer and the incident polarization direction (Figure 3c). Here, the shade of gray for each pixel is continuously modulated from 0 to 255 to achieve 8 bit pixel depth, by precisely tailoring the rotation angle of each nanoaperture unit cell. A grayscale portrait image of Einstein with a subwavelength spatial resolution of 566 nm is thus demonstrated under
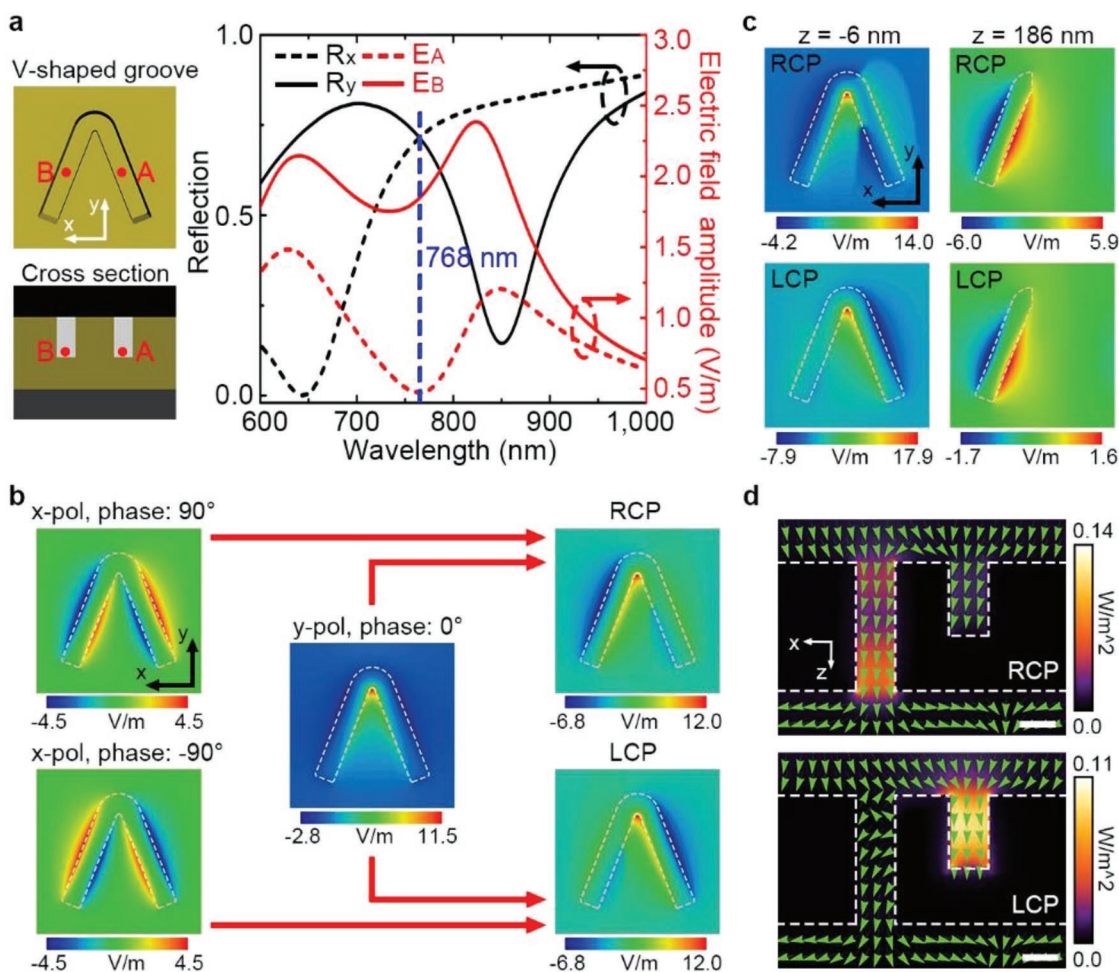
**ADVANCED
SCIENCE NEWS**
www.advancedsciencenews.com

**ADVANCED
OPTICAL
MATERIALS**
www.advopticalmat.de

Figure 2. Chiroptical analysis of the stepped V-shaped nanoaperture. a) Simulated reflection spectra of the V-shaped groove structure shown in the left panel under x-polarized and y-polarized illumination (R_x and R_y), together with the electric field amplitude acquired respectively from the center of the two halves under RCP incidence (E_A and E_B). The field points A and B are located 6 nm above the groove bottom. The V-shaped groove structure is constructed by truncating both halves of the V-shaped nanoaperture. b) Longitudinal electric field E_z distributions plotted 6 nm above the V-shaped groove structure at 768 nm under x-polarized and y-polarized illumination with certain phase delay, and the resulting E_z distributions under RCP and LCP incidence. c) E_z distributions plotted above the top surface ($z = -6$ nm) and below the bottom surface ($z = 186$ nm) of the stepped V-shaped nanoaperture in Form A under RCP and LCP illumination at 768 nm. d) Cross-section optical power flow distributions of the stepped V-shaped nanoaperture in Form A under RCP and LCP incidence at 768 nm. The background colors and field arrows indicate the magnitude and direction of the Poynting vectors. Scale bar: 50 nm.

RCP incidence with the activated subarray A. When the incident polarization is switched to LCP, the subarray A is in turn disabled, while the subarray B is functional to produce the grayscale portrait image of Curie. Figure 3d shows the partial scanning electron microscopy (SEM) image of the merged metasurface.

2.4. Chiral Grayscale Imaging

Figure 4a displays the measured results of chiral grayscale images from the merged metasurface. The operation wavelength is selected at 780 nm, which is the CDT resonance of the stepped V-shaped nanoapertures. When RCP wave is illuminated, a high-quality grayscale image of Einstein is obtained. No residual from the grayscale image of Curie is observed, indicating that the CDT value is large enough to allow the desired transmission from subarray A but effectively suppress the

unwanted transmission from subarray B. Once the proportion of RCP component among the incident beam starts to decrease, the Einstein image gets darker, while the Curie image continuously enhances. When the incident polarization is changed to purely LCP, the subarray B is completely switched on with the subarray A switched off to solely display the Curie image. The entire image evolution process is recorded in Movie S1 in the Supporting Information. In our approach, the original grayscale images are well reproduced experimentally with just slight image distortion and resolution deterioration. The discrepancies mainly come from the limited shades of gray for each pixel, which in turn stems from the resolvable angle steps for the unit cell rotation determined by the fabrication resolution of the focused ion beam system. Besides, other factors such as the imperfection of linear polarizer and quarter-wave plate in the setup, the beam quality of laser source, and the fabrication uniformity of the metasurface will also affect the final
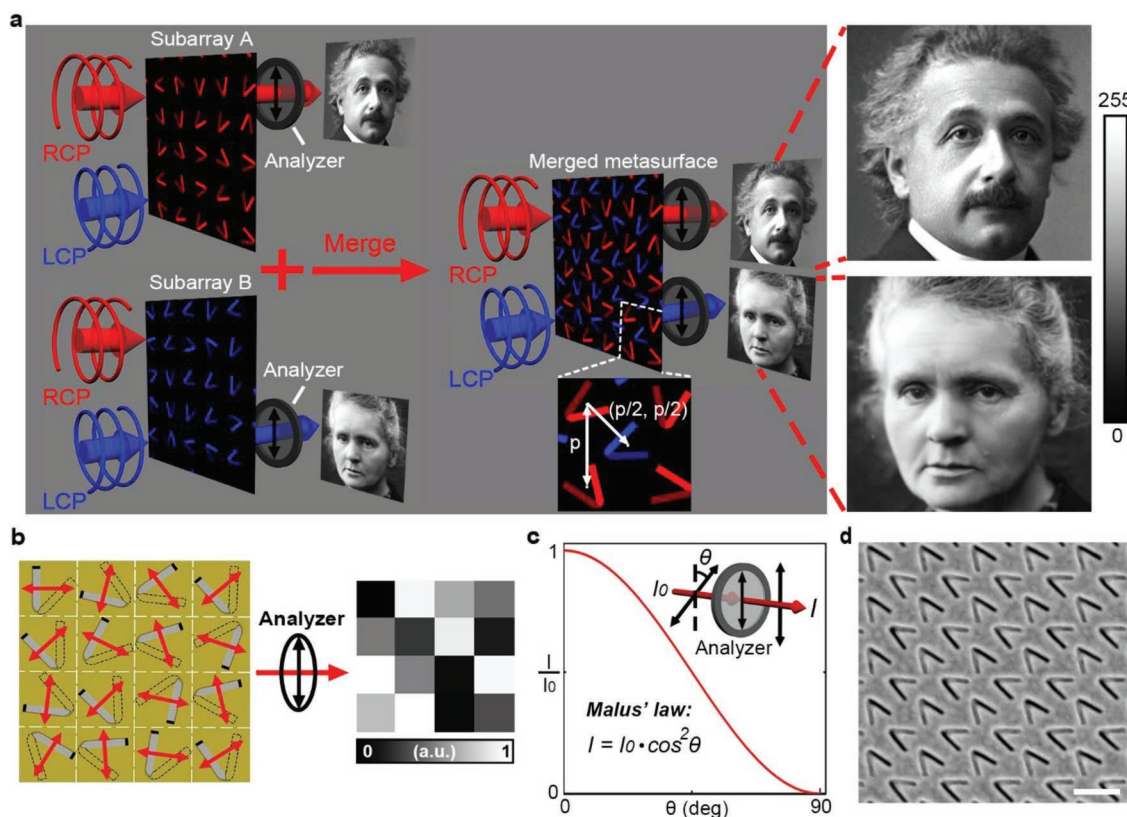
**ADVANCED
SCIENCE NEWS**

www.advancedsciencenews.com

**ADVANCED
OPTICAL
MATERIALS**

www.advopticalmat.de

Figure 3. Metasurface design for chiral grayscale subwavelength imaging. a) Schematic of the merged metasurface constructed by interlacing subarray A and subarray B with a displacement vector of $(d/2, d/2)$, where d is the unit cell period of each subarray. The subarrays A and B are composed respectively of stepped V-shaped nanoapertures in Form A and B, for generating the grayscale portrait images of Einstein and Curie in 300×300 resolution. An analyzer of linear polarizer is inserted after the metasurface to form the grayscale images. (Photographs used with permission: Close-up of Albert Einstein, 1921 (b/w photo)/Mondadori Portfolio/Bridgeman Images; Marie Curie (1867–1934), Polish physicist and chemist (b/w photo), Manuel, Henri (1874–1947)/Private Collection/Look and Learn/Elgar Collection/Bridgeman Images.) b) Schematic of a 4×4 grayscale intensity profile generated by a 4×4 array of stepped V-shaped nanoapertures through a vertically polarized analyzer following the Malus' law. The local polarization direction of the transmitted light as indicated by the red double-headed arrow is determined by the orientation of nanoaperture. c) Illustration of the Malus' law describing a linearly polarized light transmitted through an analyzer. The transmission intensity I is proportional to the square of the cosine of angle θ between the transmission axis of the analyzer and the incident polarization direction. d) Partial SEM image of the merged metasurface. Scale bar: 500 nm.

image quality. In addition, it is noted that the CDT of the stepped V-shaped nanoaperture is not perfectly unity, implying that mutual disturbance still exists between the two subarrays A and B. Furthermore, the total optical efficiency of the merged metasurface (the optical power ratio between the transmitted light to the incident light) measured before the output analyzer is about 6.8% at this wavelength, while the effective optical efficiency for the grayscale image formation measured after the analyzer is around 3.4%, which is also dependent on the angle of the output analyzer. Figure 4b shows the dependence of the captured images on the direction of output analyzer, which matches well with the simulated results in Figure S4 in the Supporting Information. If the analyzer is removed, no image is clearly observed with the grayscale images hidden in the generated polarization profiles, which can be applied for data encryption. When the analyzer is added and rotated, grayscale images are revealed and transformed, with the local image regions shining and darkening alternatively as a result of the periodicity of the cosine function. No interference between subarrays A and B are presented, further confirming the robustness of the current chiral grayscale imaging approach.

The broadband performance of chiral grayscale imaging depends on the CDT spectrum of the stepped V-shaped nanoaperture, since the linear polarization state of the transmitted light for the nanoaperture unit cell is robust against the wavelength (Figure 1e). When the operation wavelength is shifted away from the CDT resonance of 780 nm, the CDT value is continuously reduced (Figure 1d), leading to increased mutual disturbance between the two subarrays A and B. At 740 and 820 nm where the CDT equals 0.73, even though the Einstein image is primarily reproduced under RCP incidence, there are still some slight residual parts from the Curie image observed as indicated by the red arrows in **Figure 5**. The undesired residual parts also appear in the Curie image generated under LCP incidence. But for the cases of 700 and 860 nm where the CDT decreases to 0.50 and 0.53, apparent image distortions are exhibited. Accordingly, the working bandwidth of the current chiral grayscale imaging is roughly from 740 to 820 nm. The total optical efficiencies of the merged metasurface measured before the output analyzer at different wavelengths are also indicated in Figure 5.
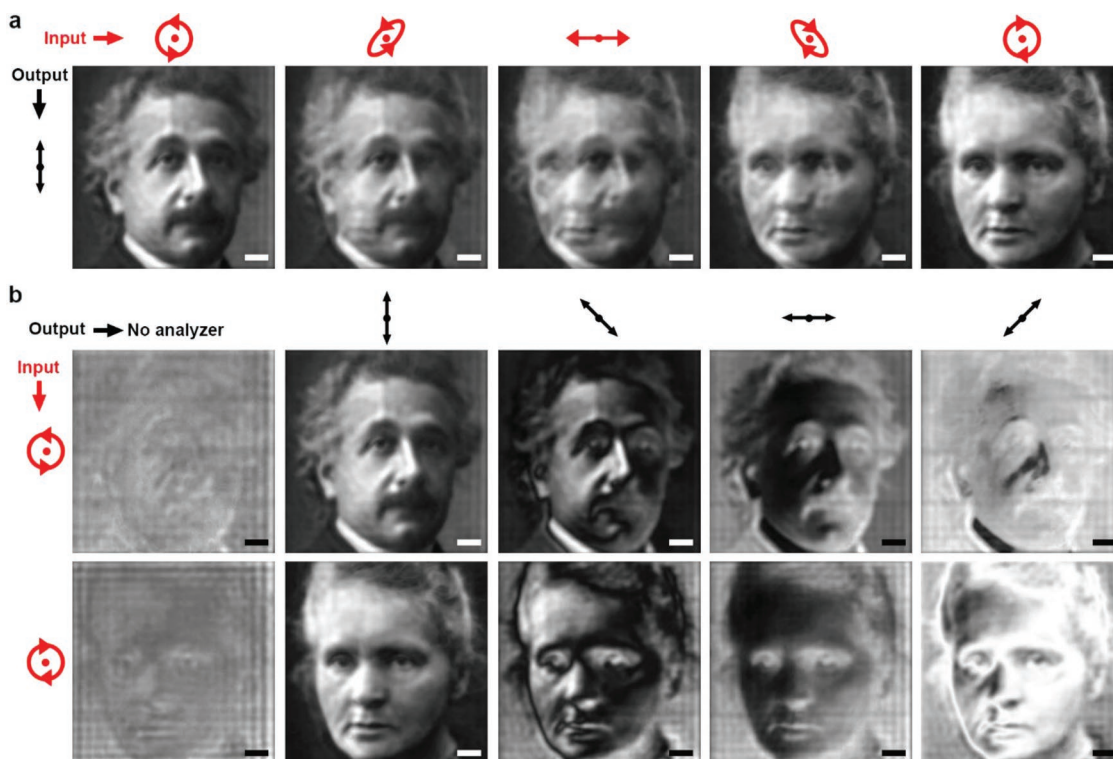
**ADVANCED
SCIENCE NEWS**
www.advancedsciencenews.com

**ADVANCED
OPTICAL
MATERIALS**
www.advopticalmat.de

Figure 4. Experimental demonstration of the chiral grayscale subwavelength imaging. a) Transmission images of the merged metasurface obtained at 780 nm with the input polarization state changed from RCP to right-handed elliptical polarization, linear polarization, left-handed elliptical polarization, and finally to LCP (from left to right). The transmission axis of the output analyzer is fixed along the vertical direction. Scale bar: 20 μm. b) Captured images at 780 nm with the output analyzer removed or rotated from 90° to 135°, 180°, and finally to 45°. The input polarization state is fixed as RCP (top) or LCP (bottom). Scale bar: 20 μm. (Photographs used with permission; details see Figure 3.)

3. Conclusion

To summarize, we have introduced the output linear polarization state of chiral nanoaperture unit cell as a new degree of freedom for realizing the chiral grayscale subwavelength imaging. The stepped V-shaped nanoapertures are proposed as unit cells to achieve linearly polarized transmission with high circular dichroism, which also inspires a simple but effective design scheme to transform achiral nanostructures to chiral nanostructures. By arranging the two enantiomeric forms of the stepped V-shaped nanoapertures into two independent subarrays and then interlacing them into one merged metasurface,
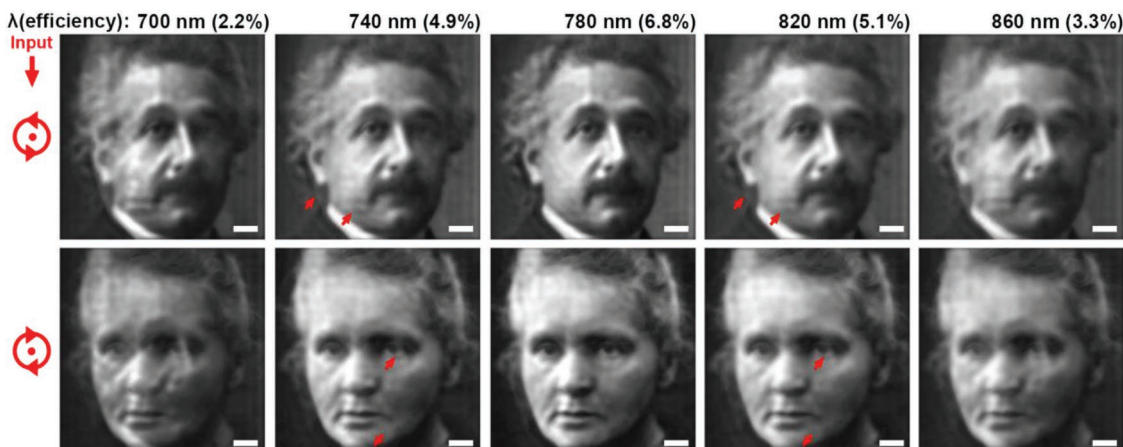

Figure 5. Broadband performance of the chiral grayscale subwavelength imaging. Images are captured at different wavelengths from 700, 740, 780, 820 nm all the way to 860 nm. The input polarization is selected as RCP (top) or LCP (bottom), and the transmission axis of the output analyzer is fixed along the vertical direction. The total optical efficiencies of the merged metasurface at different wavelengths are indicated in the brackets. Scale bar: 20 μm. The red arrows mark the evidence of mutual disturbance. (Photographs used with permission; details see Figure 3.)

spin-controlled grayscale imaging with subwavelength spatial resolution has been demonstrated. The whole grayscale range is covered with 8 bit pixel depth where the data density is orders of magnitude higher than that of the binary images generated by most of the existing chiral metamaterials or metasurfaces. The demonstrated chiral grayscale imaging approach can be applied to optical encryption and decryption, data storage, chiroptical sensing, optical communications, and optical information processing.

As final remarks, there is still a large room for further improvement of the proposed chiral imaging approach. Due to the large Ohmic loss from the gold film, the transmission efficiency of the metasurface is relatively low. To solve the problem, dielectric films with much less optical absorption, such as Si or TiO_2, can be used to replace the gold film.[7,36] Besides, when a nanostructure unit cell is rotated within the metasurface plane, a geometric phase is also locally generated. Another degree of freedom is thus provided to control the phase front of the transmitted light, which can be applied for beam shaping such as vortex beam generation[37,38] and holography.[39] In addition, the number of nanoaperture unit cells in the metasurface, and hence the number of pixels in the generated grayscale image, is currently restricted by the fabrication capacities of the focused ion beam system. Future work will be dedicated to develop a new fabrication process based on electron-beam lithography or nanoimprint technique to produce the metasurface with much larger size.

4. Experimental Section

Metasurface Fabrication: A 180 nm thick gold film was deposited on a SiO_2 substrate using an electron beam evaporator. Then, the stepped V-shaped nanoapertures were milled in the gold film using the focused ion beam system (FEI Helios Nanolab 600, Ga^+ source, 30 kV, 9.7 pA). Grayscale patterns defining the ion dose distributions of the metasurface were edited and imported into the system. The redeposition effect was considered and compensated. To obtain the cross-section SEM images, a layer of platinum was first deposited on the sample using electron beam–induced deposition. After that, a slot was milled through into the SiO_2 substrate to reveal the cross section of the stepped nanoaperture.

Imaging Setup: As shown in Figure S6 in the Supporting Information, a collimated laser beam was emitted from a tunable Ti: Sapphire oscillator (Chameleon Ultra, Coherent), transmitted through a linear polarizer and a quarter-wave plate, and then incident directly onto the metasurface sample. Uniform illumination condition was ensured for the metasurface. The transmission image from the metasurface was collected and magnified by a 10× objective lens and then captured by an infrared CCD camera. An analyzer of linear polarizer can be added and rotated in front of the camera to reveal the grayscale images.

Supporting Information

Supporting Information is available from the Wiley Online Library or from the author.

Acknowledgements

Conflict of Interest

The authors declare no conflict of interest.

Keywords

[1] M. Gu, *Advanced Optical Imaging Theory*, Vol. 75, Springer Science & Business Media, Heidelberg **2000**.

[2] N. Fang, H. Lee, C. Sun, X. Zhang, *Science* **2005**, *308*, 534.

[3] X. Ni, A. V. Kildishev, V. M. Shalaev, *Nat. Commun.* **2013**, *4*, 2807.

[4] G. Zheng, H. Muhlenbernd, M. Kenney, G. Li, T. Zentgraf, S. Zhang, *Nat. Nanotechnol.* **2015**, *10*, 308.

[5] D. Wen, F. Yue, G. Li, G. Zheng, K. Chan, S. Chen, M. Chen, K. F. Li, P. W. Wong, K. W. Cheah, E. Y. Pun, S. Zhang, X. Chen, *Nat. Commun.* **2015**, *6*, 8241.

[6] K. Huang, H. Liu, F. J. Garcia-Vidal, M. Hong, B. Luk'yanchuk, J. Teng, C. W. Qiu, *Nat. Commun.* **2015**, *6*, 7059.

[7] M. Khorasaninejad, W. T. Chen, R. C. Devlin, J. Oh, A. Y. Zhu, F. Capasso, *Science* **2016**, *352*, 1190.

[8] H. C. Liu, B. Yang, Q. Guo, J. Shi, C. Guan, G. Zheng, H. Muhlenbernd, G. Li, T. Zentgraf, S. Zhang, *Sci. Adv.* **2017**, *3*, e1701477.

[9] S. Wang, P. C. Wu, V.-C. Su, Y.-C. Lai, M.-K. Chen, H. Y. Kuo, B. H. Chen, Y. H. Chen, T.-T. Huang, J.-H. Wang, *Nat. Nanotechnol.* **2018**, *13*, 227.

[10] S. P. Rodrigues, S. Lan, L. Kang, Y. Cui, W. Cai, *Adv. Mater.* **2014**, *26*, 6157.

[11] M. Khorasaninejad, W. T. Chen, A. Y. Zhu, J. Oh, R. C. Devlin, D. Rousso, F. Capasso, *Nano Lett.* **2016**, *16*, 4595.

[12] M. Khorasaninejad, A. Ambrosio, P. Kanhaiya, F. Capasso, *Sci. Adv.* **2016**, *2*, e1501258.

[13] L. Kang, S. P. Rodrigues, M. Taghinejad, S. Lan, K. T. Lee, Y. Liu, D. H. Werner, A. Urbas, W. Cai, *Nano Lett.* **2017**, *17*, 7102.

[14] Y. Chen, J. Gao, X. Yang, *Nano Lett.* **2018**, *18*, 520.

[15] Q. Wang, E. Plum, Q. Yang, X. Zhang, Q. Xu, Y. Xu, J. Han, W. Zhang, *Light: Sci. Appl.* **2018**, *7*, 25.

[16] Y. Chen, X. Yang, J. Gao, *Light: Sci. Appl.* **2018**, *7*, 84.

[17] Y. Chen, J. Gao, X. Yang, *Laser Photonics Rev.* **2018**, *12*, 1800198.

[18] L. D. Barron, *Molecular Light Scattering and Optical Activity*, Cambridge University Press, Cambridge **2004**.

[19] D. K. Smith, *Chem. Soc. Rev.* **2009**, *38*, 684.

[20] X. Yin, M. Schaferling, B. Metzger, H. Giessen, *Nano Lett.* **2013**, *13*, 6238.

[21] V. E. Ferry, M. Hentschel, A. P. Alivisatos, *Nano Lett.* **2015**, *15*, 8336.

[22] Y. Hwang, B. Hopkins, D. Wang, A. Mitchell, T. J. Davis, J. Lin, X.-C. Yuan, *Laser Photonics Rev.* **2017**, *11*, 1700216.

[23] W. Ma, F. Cheng, Y. Liu, *ACS Nano* **2018**, *12*, 6326.

[24] F. Yue, C. Zhang, X.-F. Zang, D. Wen, B. D. Gerardot, S. Zhang, X. Chen, *Light: Sci. Appl.* **2018**, *7*, 17129.

[25] X. Zang, F. Dong, F. Yue, C. Zhang, L. Xu, Z. Song, M. Chen, P. Y. Chen, G. S. Buller, Y. Zhu, *Adv. Mater.* **2018**, *30*, 1707499.

[26] C. Menzel, C. Rockstuhl, F. Lederer, *Phys. Rev. A* **2010**, *82*, 053811.

[27] V. K. Valev, J. J. Baumberg, C. Sibilia, T. Verbiest, *Adv. Mater.* **2013**, *25*, 2517.

[28] M. Hentschel, M. Schaferling, X. Duan, H. Giessen, N. Liu, *Sci. Adv.* **2017**, *3*, e1602735.

[29] G. Biener, A. Niv, V. Kleiner, E. Hasman, *Opt. Lett.* **2005**, *30*, 1096.

[30] Y. Chen, X. Duan, M. Matuschek, Y. Zhou, F. Neubrech, H. Duan, N. Liu, *Nano Lett.* **2017**, *17*, 5555.

[31] X. Chen, Z. Huang, S.-Y. Chen, K. Li, X.-Q. Yu, L. Pu, *J. Am. Chem. Soc.* **2010**, *132*, 7297.

[32] A. Silva, F. Monticone, G. Castaldi, V. Galdi, A. Alù, N. Engheta, *Science* **2014**, *343*, 160.

[33] X. Ni, S. Ishii, A. V. Kildishev, V. M. Shalaev, *Light: Sci. Appl.* **2013**, *2*, e72.

[34] S. Zu, T. Han, M. Jiang, F. Lin, X. Zhu, Z. Fang, *ACS Nano* **2018**, *12*, 3908.

[35] Z. Ruan, M. Qiu, *Phys. Rev. Lett.* **2006**, *96*, 233901.

[36] D. Lin, P. Fan, E. Hasman, M. L. Brongersma, *Science* **2014**, *345*, 298.

[37] F. Yue, D. Wen, C. Zhang, B. D. Gerardot, W. Wang, S. Zhang, X. Chen, *Adv. Mater.* **2017**, *29*, 1603838.

[38] Y. Chen, X. Yang, J. Gao, *Adv. Opt. Mater.* **2018**, *6*, 1800646.

[39] Z. L. Deng, J. Deng, X. Zhuang, S. Wang, K. Li, Y. Wang, Y. Chi, X. Ye, J. Xu, G. P. Wang, R. Zhao, X. Wang, Y. Cao, X. Cheng, G. Li, X. Li, *Nano Lett.* **2018**, *18*, 2885.